

A low-mass line-rich core found in Massive Star-forming Region IRAS 16351-4722

MEIZHU LIU,¹ SHENG-LI QIN,¹ TIE LIU,² MENGYAO TANG,³ SHENG-YUAN LIU,⁴ LI CHEN,¹ CHUANSHOU LI,¹
HONGQIONG SHI,¹ XIAOHU LI,⁵ TIANWEI ZHANG,⁶ KEN'ICHI TATEMATSU,⁷ FENGWEI XU,^{8,9} AND YUEFANG WU⁹

¹*School of Physics and Astronomy, Yunnan University, Kunming 650091, People's Republic of China*

²*Shanghai Astronomical Observatory, Chinese Academy of Sciences, 80 Nandan Road, Shanghai 200030, People's Republic of China*

³*Institute of Astrophysics, School of Physics and Electronic Science, Chuxiong Normal University, Chuxiong 675000, People's Republic of China*

⁴*Institute of Astronomy and Astrophysics, Academia Sinica, 11F of Astronomy-Mathematics Building, AS/NTU No. 1, Section 4, Roosevelt Road., Taipei 10617, Taiwan*

⁵*Xinjiang Astronomical Observatory, Chinese Academy of Sciences, Urumqi, China*

⁶*I. Physikalisches Institut, Universität zu Köln, Zùlpicher Straße 77, 50937 Köln, Germany*

⁷*Nobeyama Radio Observatory, National Astronomical Observatory of Japan, National Institutes of Natural Sciences, Nobeyama, Minamimaki, Minamisaku, Nagano 384-1305, Japan*

⁸*Kavli Institute for Astronomy and Astrophysics, Peking University, 5 Yi-heyuan Road, Haidian District, Beijing 100871, China*

⁹*Department of Astronomy, School of Physics, Peking University, Beijing 100871, People's Republic of China*

ABSTRACT

We present ALMA sub-arcsecond-resolution observations of both continuum and molecular lines at 345 GHz towards the massive star-forming region IRAS 16351-4722 (hereafter I16351). A total of 12 dust cores were detected based on high spatial resolution observations of the continuum. Among them, a high-mass core (11.6 M_⊙) and a low-mass core (1.7 M_⊙) show abundant molecular line emissions. 164 molecular transitions from 29 species and 104 molecular transitions from 25 species are identified in the high-mass and low-mass cores, respectively. Complex organic molecules (COMs) such as CH₃OH, CH₃OCHO, CH₃OCH₃, C₂H₅OH, and C₂H₅CN are detected in the two cores. Under the assumption of local thermodynamic equilibrium (LTE), rotational temperatures and column densities of the COMs are derived with the XCLASS software. The maximum rotation temperature values in the low-mass core and the high-mass core were found to be approximately 130 K and 198 K, respectively. Additionally, the line widths in the high-mass core are larger than those in the low-mass one. Abundant complex organic molecular line transitions, high gas temperatures, and smaller line widths indicate the presence of a low-mass line-rich core in the massive star formation region for the first time, while the high-mass line-rich core shows hot core property. When comparing the molecular abundances of CH₃OH, CH₃OCHO, CH₃OCH₃ and C₂H₅OH of the two cores with other hot cores and hot corinos reported in the literature, we further confirm that both a hot core and a low-mass line-rich core are simultaneously detected in I16351.

Keywords: star: formation; ISM: astrochemistry; line: identification; methods: observational; ISM: abundances

1. INTRODUCTION

The development of radio telescopes has facilitated in-depth investigations of interstellar molecules (e.g., [Tercero et al. 2018](#); [Bonfand et al. 2019](#); [Pagani et al. 2019](#)).

So far, about 300 molecules¹ composed of 16 different elements, with atomic numbers ranging from 2 to 70, have been detected in interstellar space. Complex organic molecules (COMs), which consist of six or more atoms containing carbon atoms, serve as valuable indicators of the physical conditions and history of their

Corresponding author: Meizhu Liu
lmz@mail.ynu.edu.cn

¹ <https://cdms.astro.uni-koeln.de/classic/molecules>

sources through their spectra and chemical properties (Herbst & van Dishoeck 2009). COMs are mostly detected in hot cores and hot corinos (Jørgensen et al. 2020), but also on the surface of the embedded disks where the temperature is warm ($\gtrsim 100$ K; (e.g., Lee et al. 2017)). Jets and outflows can also produce the emission of COMs by sputtering and/or shock chemical events (e.g., Arce et al. 2008; Lefloch et al. 2017).

The hot core is characterized by a dense ($\gtrsim 10^7$ cm $^{-3}$) region on scales < 0.1 pc, abundant molecular line emissions with high gas temperatures ($\gtrsim 100$ K) and high molecular abundances (Kurtz et al. 2000; Herbst & van Dishoeck 2009). Hot core observations in massive star-forming regions have been promoted by the millimetre/submillimetre interferometric arrays greatly (Liu et al. 2002; Remijan et al. 2004; Qin et al. 2010, 2015; Beuther et al. 2005; Sánchez-Monge et al. 2014; Sakai et al. 2013, 2018; Hernández-Hernández et al. 2014; Belloche et al. 2016, 2019; Rong et al. 2016; Bonfand et al. 2017; Pagani et al. 2017; Rivilla et al. 2017; Ahmadi et al. 2018; Guzmán et al. 2018; Tercero et al. 2018; Bøgelund et al. 2019; Csengeri et al. 2019; Xue et al. 2019; Mottram et al. 2020; Ligterink et al. 2020; Taniguchi et al. 2020; Law et al. 2021; van der Walt et al. 2021). Hot corino sources are characterized by localized zones that surround low-mass to intermediate-mass protostars, and they have warm gas temperatures (~ 100 K), and compact COM emissions (~ 100 AU) (Ceccarelli 2004). Since the first proposal of the definition of “hot corino” (Ceccarelli 2004), only about a couple of tens of hot corino sources have been discovered (Hsu et al. 2020). Recently, Belloche et al. (2020) observed 26 solar-type star-forming regions, in which warm methanol is detected in 12 sources. Hsu et al. (2020, 2022) reported the detection of 11 hot corino sources among 56 Class 0/I protostellar cores from the ALMA observations of Orion Planck Galactic Cold Clumps. In summary, high-resolution interferometer observations expand the sample size of hot corinos.

IRAS 16351-4722 (hereafter I16351) is located at a distance of 3.02 kpc with a high clump mass of $1.58 \times 10^3 M_{\odot}$ and infrared bolometric luminosity of $7.9 \times 10^4 L_{\odot}$ (Liu et al. 2020). ALMA observations of CO (3-2) suggested outflow motion in this region (Baug et al. 2021). CO (4-3) line in I16351 shows a blue profile, characterized by an asymmetric parameter of -0.76 and a virial parameter of 1.93, indicating a global collapse within this region (Yue et al. 2021). These observations suggested that I16351 is an active massive star-forming region. More recently, Qin et al. (2022) identified the emissions of C₂H₅CN, CH₃OCHO, and CH₃OH in the 3 mm band, with rotational temperatures exceeding 100

K, implying the presence of a hot core in I16351. Therefore, I16351 is a valuable target for studying the physical and chemical conditions involved in the massive star-forming processes.

In this work, we present high spatial resolution ALMA observations toward I16351 at 345 GHz. Section 2 introduces ALMA Band 7 observations and data reduction. We describe the observational results in Section 3. In Section 4, we discuss the results of the study, and our conclusions are summarized Section 5.

2. OBSERVATIONS

This study utilized the ALMA Band 7 observation data (Project ID: 2017.1.00545S, Project PI: Liu Tie). The data collection took place on May 18th to 20th, 2018, during ALMA Cycle 5. A total of 43 12-meter array were deployed, using the C43-1 array configuration. The Band 7 observational data covered four spectral windows (SPWs 31, 29, 27, and 25) that encompassed the following frequency ranges: (i) 342.36–344.24 GHz, (ii) 344.25–346.09 GHz, (iii) 356.60–357.07 GHz, and (iv) 354.27–354.74 GHz. SPWs 25 and 27 have a narrow bandwidth of 468.75 MHz and a spectral resolution of 0.24 km s $^{-1}$. SPWs 29 and 31 have a broad bandwidth of 1875 MHz and a spectral resolution of 0.98 km s $^{-1}$, which intend to cover a broad range of spectral lines. The purpose of this article is to analyze chemistry using molecular spectra, so the main analysis focuses at the broad spectral window SPWs 31 and SPWs 29. The observations were conducted using the Mosaic mode, providing an approximate field of view of 46'' at 345 GHz. The phase center coordinates were R.A.(J2000) = 16^h38^m49^s and Decl.(J2000) = $-47^{\circ}28'03''$. Data processing was performed using the Common Astronomy Software Applications Package (CASA version 5.3.0) (McMullin et al. 2007). The flux and bandpass calibration was initially applied using J1924-2914, J1427-4206, and J1517-2422. The phase calibration was carried out using J1650-5044. Imaging was carried out with `tclean` task and `robust=0.5` was used to balance the weight between the long and short baseline data. To improve the final image, a self-calibration operation was performed on both the continuum and is applied to the solution of self-calibration from the continuum on the line data. The 870 μ m continuum data were extracted from line-free channels. The final synthesized beam size is 0.8'' \times 0.7''. The continuum RMS noise level is 1.3 mJy beam $^{-1}$, and the average line sensitivity is 5.05 mJy beam $^{-1}$ per channel.

3. RESULTS

3.1. Continuum

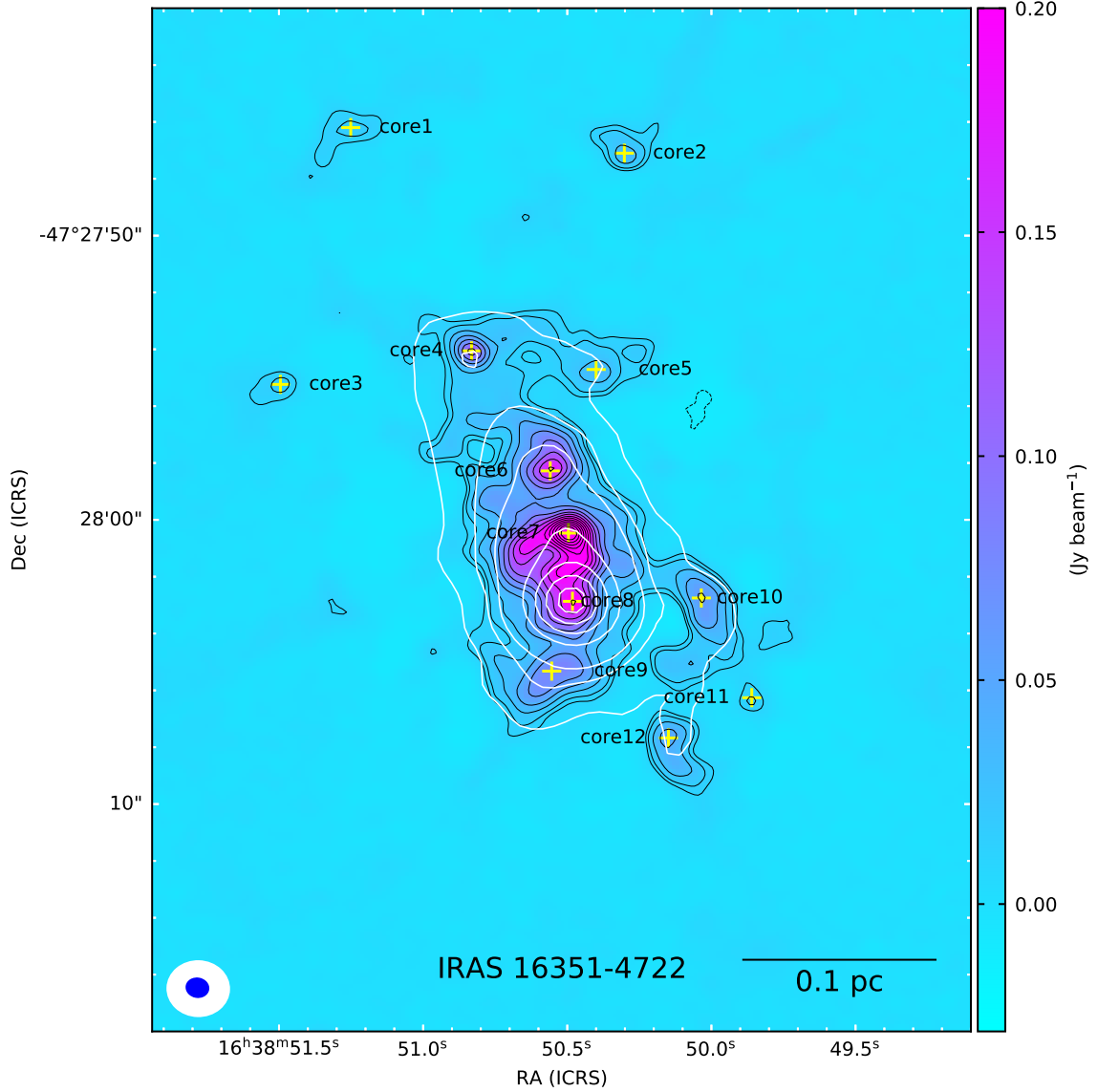


Figure 1. 870 μm continuum emission map of I16351 from the ALMA Band 7 observations in color scale and black contours overlaid with 3 mm continuum in white contours. The synthesized beam size is shown in the bottom-left corner. The black contours start at a level of $8\sigma=0.0104 \text{ Jy beam}^{-1}$ and increase in the following power-law function $D=4\times N^p+8$, where D is the dynamical range of the intensity map as follows: 0.0104, 0.0156, 0.0267, 0.0423, 0.0614, 0.0841, 0.1099, 0.1386, 0.1701, 0.2043, 0.2411, 0.2803, 0.3219, 0.3658, 0.4119 Jy beam^{-1} , the p of 1.6 is the power index, $N=15$ is the number of contours used. The white contour levels are [3%, 6%, 10%, 30%, 50%, 70%, 90%] \times peak integrated intensities ($F_{\text{peak}} = 0.1193 \text{ Jy beam}^{-1} \text{ km}^{-1}$). The crosses show the peak positions of each core.

Previous ALMA 3 mm observations with angular resolution $1.2''\text{-}1.9''$ (Liu et al. 2020) only detected one continuum core (Qin et al. 2022). In Figure 1, 12 continuum cores have been detected in our ALMA high-angular continuum map. From top to bottom, we name these cores from core 1 to core 12. The continuum emission shows a complicated morphology, accompanied by a north-south extended structure. Core 7 and 8 are located in the center of the region. The brightest core is core 7 and the second is core 6. The other cores are lo-

cated away from the three cores. The 870 μm continuum emission map in color scale and black contour, overlaid with 3 mm continuum in white contour. The white contour of the 3 mm image shows a simple morphology with a single core detected (Qin et al. 2022). The emission peak of core 8 in this work is consistent with the peak position of the 3 mm continuum.

We performed a two-dimensional Gaussian fitting to the 12 cores. The positions, deconvolved source sizes, peak intensities, and flux densities of these cores are

listed in Table 1. According to Table 1, the flux densities range from 33 to 3010 mJy. Additionally, the peak intensities range from 17 to 320 mJy beam⁻¹. Among all cores, core 7 has the largest flux density and peak intensity.

To estimate the masses of the cores, we followed the procedure of Hildebrand (1983) for an optically thin emission with a single temperature:

$$M_{\text{core}} = \frac{D^2 S_\nu \eta}{\kappa_\nu B_\nu(T_d)}, \quad (1)$$

where S_ν is the continuum integrated flux, D is the distance to the source, η is the gas-to-dust ratio (100), and $B_\nu(T_d)$ is the Planck function at the dust temperature (T_d). κ_ν is the dust mass absorption coefficient of 1.89 cm²g⁻¹ at 870 μ m in Ossenkopf & Henning (1994), assuming grains with thin ice mantles and a gas density of 10⁻⁶ cm⁻². The dust temperature is assumed to be equal to CH₃OCHO rotational temperatures in hot regions or H₂CS rotational temperatures in warm regions because H₂CS has been observed towards cold molecular clouds, protostellar cores, hot cores, circumstellar envelopes, and protoplanetary discs (Spezzano et al. 2022).

We calculate the source-averaged H₂ column density according to Schuller et al. (2009), assuming the dust emission at 870 μ m is optically thin:

$$N(\text{H}_2) = \frac{S_\nu \eta}{\mu m_H \Omega \kappa_\nu B_\nu(T_d)}, \quad (2)$$

where Ω is the solid angle subtended by the source, μ is the mean molecular weight of the molecular cloud, which we assume to be equal to 2.8 (Kauffmann et al. 2008), and m_H is the mass of a hydrogen atom. The mean optical depth of the continuum cores can be calculated by (e.g., Frau et al. 2010; Gieser et al. 2021):

$$\tau_{870} = -\ln\left[1 - \frac{S_\nu}{\Omega B_\nu(T_d)}\right] \quad (3)$$

τ_{870} of the 12 cores is of the order of 10⁻², therefore the optically thin assumption is reasonable. From Table 1, M_{core} is in the range of 0.3 M_⊙ – 11.6 M_⊙. N_{H_2} ranges from 4.0 × 10²² cm⁻² – 2.3 × 10²³ cm⁻².

3.2. Molecular line identification

We extract the spectral lines towards each core, and find that core 7 with a high mass of 11.6 M_⊙ and core 4 with a low mass of 1.7 M_⊙ have rich line emission when compared to the other cores. In this work, we focused on these line-rich cores for further analysis. To identify the observed molecular line transitions, we used the eX-

tended CASA Line Analysis Software Suite (XCLASS²; (Möller et al. 2017)). XCLASS accesses the Cologne Database for Molecular Spectroscopy (CDMS³; (Müller et al. 2005)) and the Jet Propulsion Laboratory molecular databases (JPL⁴; (Pickett et al. 1998)). We assumed that the molecular gas was in local thermodynamic equilibrium (LTE) and used the XCLASS program for the line identification. The input parameters for the modelling include the source size, line velocity width, velocity offset, rotation temperature, and column density (Möller et al. 2017). Figure 2 illustrates the molecular identification results of the two cores. Each plot shows the molecular line flux changing with frequency in the SPW 31 and SPW 29 spectral windows, and the molecular names are marked above the lines. From Figure 2, one can see that the line fluxes in the high-mass core are generally much higher than those in the low-mass core. The line widths (FWHMs) of the high-mass core are broader than those of the low-mass core (see also Section 4). In total, 164 molecular line transitions from 29 species were identified in the high-mass core, while 104 molecular line transitions from 25 species were identified in the low-mass core. The common molecules detected in both the high-mass and low-mass cores include CH₃OCHO, CH₃OCHO v₁₈=1, CH₃OCH₃, CH₃OH, H₂CS, CH₃COCH₃, C₂H₅CN, t-HCOOH, H₂CCO, ¹³CH₃OH, aGg'-(CH₂OH)₂, CH₃CHO, C₂H₅OH, HC₃N and SO₂. Formamide (NH₂CHO), the simplest possible amide that has been considered a potential prebiotic molecule and a potential precursor to heavier COMs, such as amino acids (e.g., López-Sepulcre et al. 2015; López-Sepulcre et al. 2019), is also identified in both the high-mass and low-mass cores. ³⁴SO₂, C₂H₃CN, C₂H₃CN v₁₁=1 and CH₃C₄H are only observed in the high-mass core. CH₃C₃N, CH₃SH v₁₂=1 and c-H₂C₃O are only detected in the low-mass core. Therefore, the differences in molecular compositions appear to be caused by differences in their chemical properties between the high-mass and the low-mass core.

3.3. Gas distribution

We have detected numerous molecules in the two cores, and selected representative molecules for imaging their spatial distributions. Figure 3 shows the integrated intensity maps of the oxygen-, nitrogen- and sulfur-bearing molecules. Gas emissions of CH₃OCHO, ¹³CH₃OH, CH₃OH, CH₃COCH₃, HCOOH, CH₃CHO, C₂H₅CN, NH₂CHO, HC₃N, H₂CS, and SO₂ are dis-

² <https://xclass.astro.uni-koeln.de>

³ <http://cdms.de>

⁴ <http://jpl.de>

Table 1. Parameters of Continuum Sources

Name	R.A. (J2000)	Decl. (J2000)	Peak Intensity (mJy beam ⁻¹)	Integrated Flux ^a (mJy)	Source Size ^a ("×")	M _{core} M _⊙	N _{H₂} cm ⁻²	T ^b K	Catalog
core 1	16:38:51.2	-47:27:46.2	18(2)	111(12)	2.4 × 1.1	3.0(0.7)	7.6 × 10 ²² (0.8)	30(6)	Dust
core 2	16:38:50.3	-47:27:47.1	34(3)	95(10)	1.1 × 0.8	2.6(0.6)	2.0 × 10 ²³ (0.2)	30(6)	Dust
core 3	16:38:51.5	-47:27:55.2	18(4)	65(4)	1.4 × 0.9	1.8(0.4)	9.4 × 10 ²² (0.6)	30(6)	Dust
core 4	16:38:50.8	-47:27:54.1	113(3)	220(9)	0.8 × 0.6	1.7(0.2)	2.3 × 10 ²³ (0.09)	90(9)	CH ₃ OCHO
core 5	16:38:50.4	-47:27:54.7	35(1)	146(4)	1.5 × 1.0	4.0(0.8)	1.8 × 10 ²³ (0.05)	30(6)	Dust
core 6	16:38:50.6	-47:27:58.1	144(10)	1024(79)	1.9 × 1.6	8.0(1.3)	1.7 × 10 ²³ (0.1)	87(12)	H ₂ CS
core 7	16:38:50.5	-47:28:00.8	320(45)	3010(470)	2.2 × 1.9	11.6(1.9)	1.9 × 10 ²³ (0.4)	170(10)	CH ₃ OCHO
core 8	16:38:50.5	-47:28:02.8	199(4)	1511(36)	2.1 × 1.6	11.4(1.3)	2.3 × 10 ²³ (0.05)	91(10)	CH ₃ OCHO
core 9	16:38:50.6	-47:28:05.3	79(1)	597(10)	2.7 × 1.2	7.6(0.6)	1.6 × 10 ²³ (0.03)	56(4)	H ₂ CS
core 10	16:38:50.0	-47:28:02.8	63(4)	378(23)	2.0 × 0.9	4.6(0.6)	1.7 × 10 ²³ (0.1)	58(7)	H ₂ CS
core 11	16:38:49.9	-47:28:06.2	17(1)	33(1)	0.8 × 0.6	0.3(0.02)	4.0 × 10 ²² (0.1)	78(5)	H ₂ CS
core 12	16:38:50.1	-47:28:07.7	49(4)	170(9)	1.3 × 0.9	2.4(0.6)	1.4 × 10 ²³ (0.07)	51(12)	H ₂ CS

NOTE—^a The total flux density and deconvolved size of each core are obtained from 2D Gaussian fitting to 870 μm continuum. ^b The dust temperature used is the excitation temperature of H₂CS or CH₃OCHO molecules. If there are no H₂CS or CH₃OCHO molecules in the core, we assume that the core’s dust temperature is 30K (Liu et al. 2020).

tributed over both the low-mass and the high-mass continuum cores, while C₂H₃CN only concentrated on the high-mass core, as shown in Figure 3. By comparing the above 11 molecular gas distributions in both two cores, the distributions of sulfur-bearing molecules are more extended, and nitrogen-bearing molecules show compact structures.

4. DISCUSSION

We modelled the observed spectra using the XCLASS suite. The software contains an interface for the model optimizer package MAGIX (Modelling and Analysis Generic Interface for eXternal numerical codes; (Möller et al. 2013)), and finds the best solutions of parameters and provides the corresponding error estimation by using different optimization algorithms (Genetic Algorithm (GA), Levenberg-Marquardt (LM) and Markov Chain Monte Carlo (MCMC) algorithms). The parameters derived from the best-fitting models, the rotational temperature T_{rot} and total column density N_{tot} of the identified molecules are summarized in Table 2 for the high-mass and low-mass cores. The rotational temperatures of molecules range from 93 to 198 K in the high-mass core and from 50 to 130 K in the low-mass core. The column densities range from 2.5 × 10¹⁵ cm⁻² to 4.0 × 10¹⁷ cm⁻² in the high-mass core and 7.0 × 10¹³ cm⁻² to 2.0 × 10¹⁶ cm⁻² in the low-mass core. The line widths range from 4.5 to 9.0 km s⁻¹ in the high-mass core, and from 1.5 to 3.0 km s⁻¹ in the low-mass core. Considering the effect on linewidth due to spectral resolution (0.98 km s⁻¹), the deconvolved line width is calculated by $\text{FWHM}_{\text{decon}} = \sqrt{\text{FWHM}^2 - \Delta V^2}$, where FWHM is the fitted linewidth convolved with spectral resolution ΔV². Their ranges become 1.13 to 2.83 km s⁻¹ in the low-mass core and 4.39 to 8.95 km s⁻¹ in the high-mass core.

The fractional abundance of a specific molecule can be obtained by $f_{\text{H}_2} = N_{\text{tot}}/N_{\text{H}_2}$ (N_{H₂}=2.3(0.04) × 10²³ cm⁻² for the low-mass line-rich core and N_{H₂}=1.9(0.2) × 10²³ cm⁻² for the hot core). The fractional abundances of different species in the two cores are presented in Table 2 according to their abundances in declining order. Together with small mass, abundant line emissions from COMs, high gas temperature, narrow line width, we suggest that the low-mass core in I16351 is a low-mass line-rich core in high-mass star-forming region. The position of the high-mass core is consistent with the hot core position observed by Qin et al. (2022). CH₃OH abundance in the high-mass core is approximately 10⁻⁶ (Table 2), and abundances of other COMs (~ 10⁻⁸–10⁻⁷) are reproduced in a hot core model with temperature above 100 K (Garrod 2013), which suggest an active hot core chemistry scenario in the high-mass core (Taniguchi et al. 2019, 2020).

We have also compiled molecular abundances of CH₃OCHO, CH₃OCH₃, CH₃OH, C₂H₅OH, H₂CCO and C₂H₅CN and CH₃OCHO, CH₃OCH₃, CH₃OH, C₂H₅OH, NH₂CHO and CH₃CHO in some hot cores and hot corinos in Table B1 and Table B2 to compare with our results. Figure 4 shows the molecular abundance of two cores in I16351 and other hot cores and hot corinos. We find that the fractional abundances of the hot core in I16351 are similar to the average values of other hot cores and the molecular abundances of the low-mass line-rich core in I16351 are similar to the average values of other hot corinos, confirming that a low-mass line-rich core and a hot core are detected in the high-mass star-forming region I16351. CH₃OH has high fractional abundances in hot cores and hot corinos. H₂CCO and NH₂CHO have the lowest fractional abundances in hot cores and hot corinos. Meanwhile, it

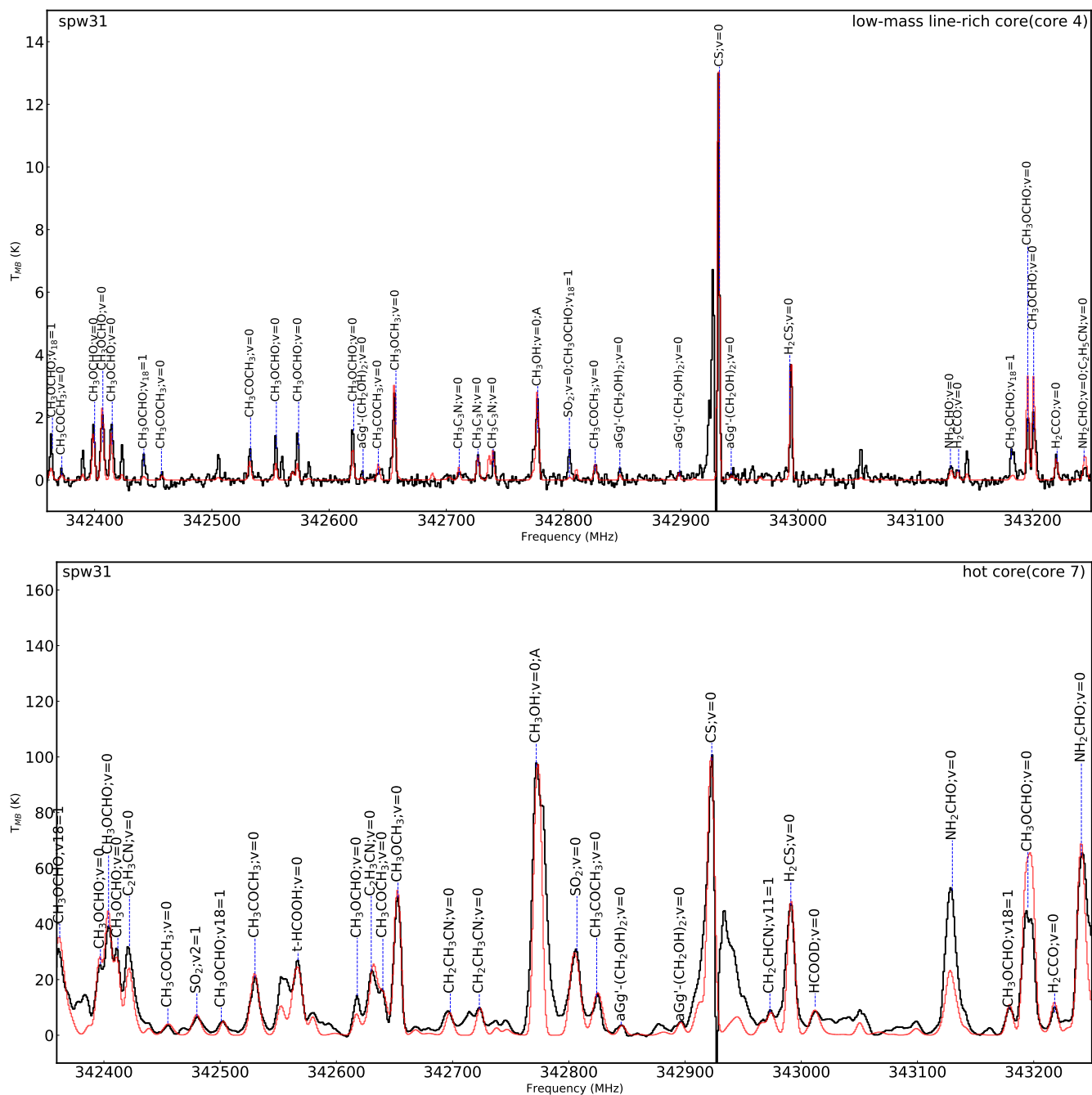


Figure 2. Sample spectra in spw31 and spw29 toward the hot core and the low-mass line-rich core. The segments of spw31 and spw29 cover the frequency range from 342 to 346 GHz. The frequency scale is in terms of the rest frequency. The black curves are the observed spectra and the red curves indicate the simulated LTE spectra.

can be seen from Figure 4 that abundances of CH_3OCH_3 are generally higher than those of $\text{C}_2\text{H}_5\text{OH}$ in hot cores. The abundances of the two species are nearly the same for hot corinos. From Figure 4 and Tables B1 and B2, the abundances in the hot core are generally higher than those in the low-mass core by approximately 1–2 orders of magnitude.

Figure 5 compares the molecular abundance with respect to CH_3OH of the low-mass core in I16351 with other hot corinos in Table B2. Methyl formate (CH_3OCHO) is the most abundant COM with relative abundances of 1.6%–54%, followed by dimethyl ether (CH_3OCH_3) (1%–36%) and ethanol ($\text{C}_2\text{H}_5\text{OH}$) (1%–32%). Other COMs are detected with relative abundances lower than 10%: Formamide (NH_2CHO)

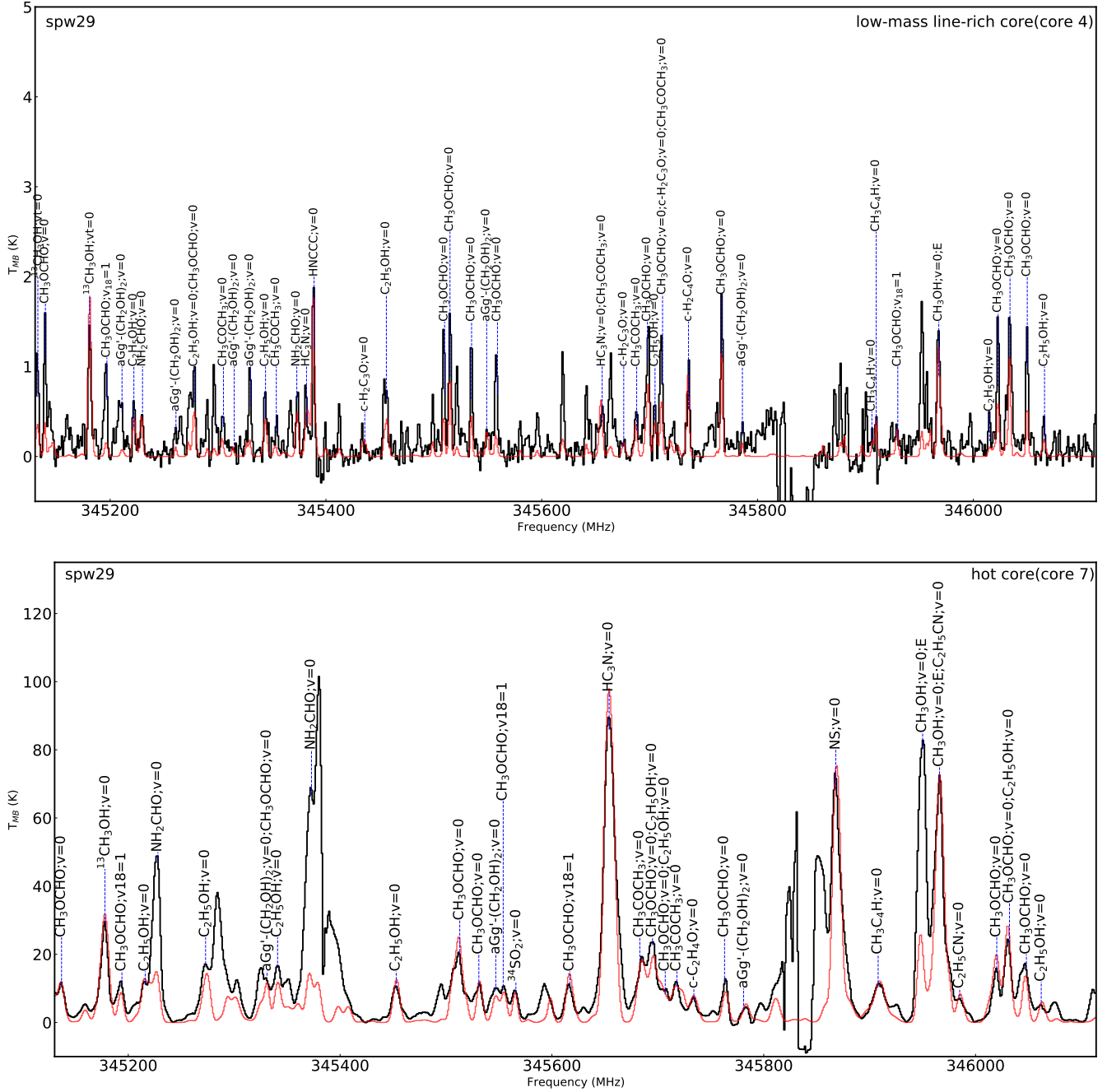


Figure 2. (continued)

rich core is detected in the massive star-forming region.

4. The two line-rich cores in I16351 reside in the same region and have different chemical properties, implying that the different chemistry between the two cores are likely influenced by their physical conditions.

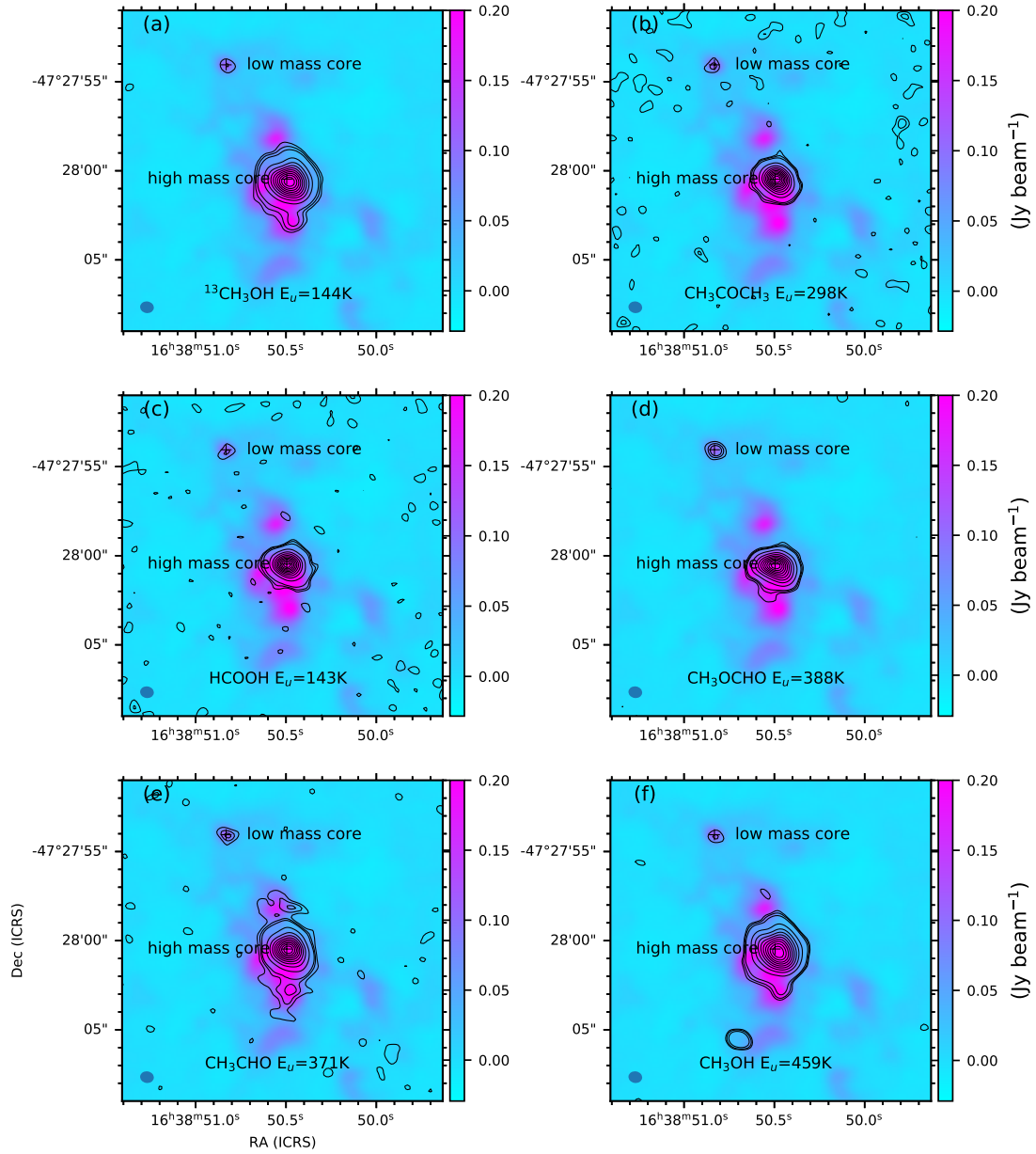


Figure 3. Spatial distributions of O-, N- and S-bearing molecules. The black contour levels are [1%, 2%, 3%, 10%, 20%, 30%, 40%, 50%, 60%, 70%, 80%, 90%] \times peak integrated intensities (F_{peak}). The color grey scale background shows the continuum emission at 0.87 mm. The synthetic beam for the continuum is indicated in the bottom left corner by the blue ellipse. The value of upper-level energy E_u for each species is shown in the bottom of each panel.

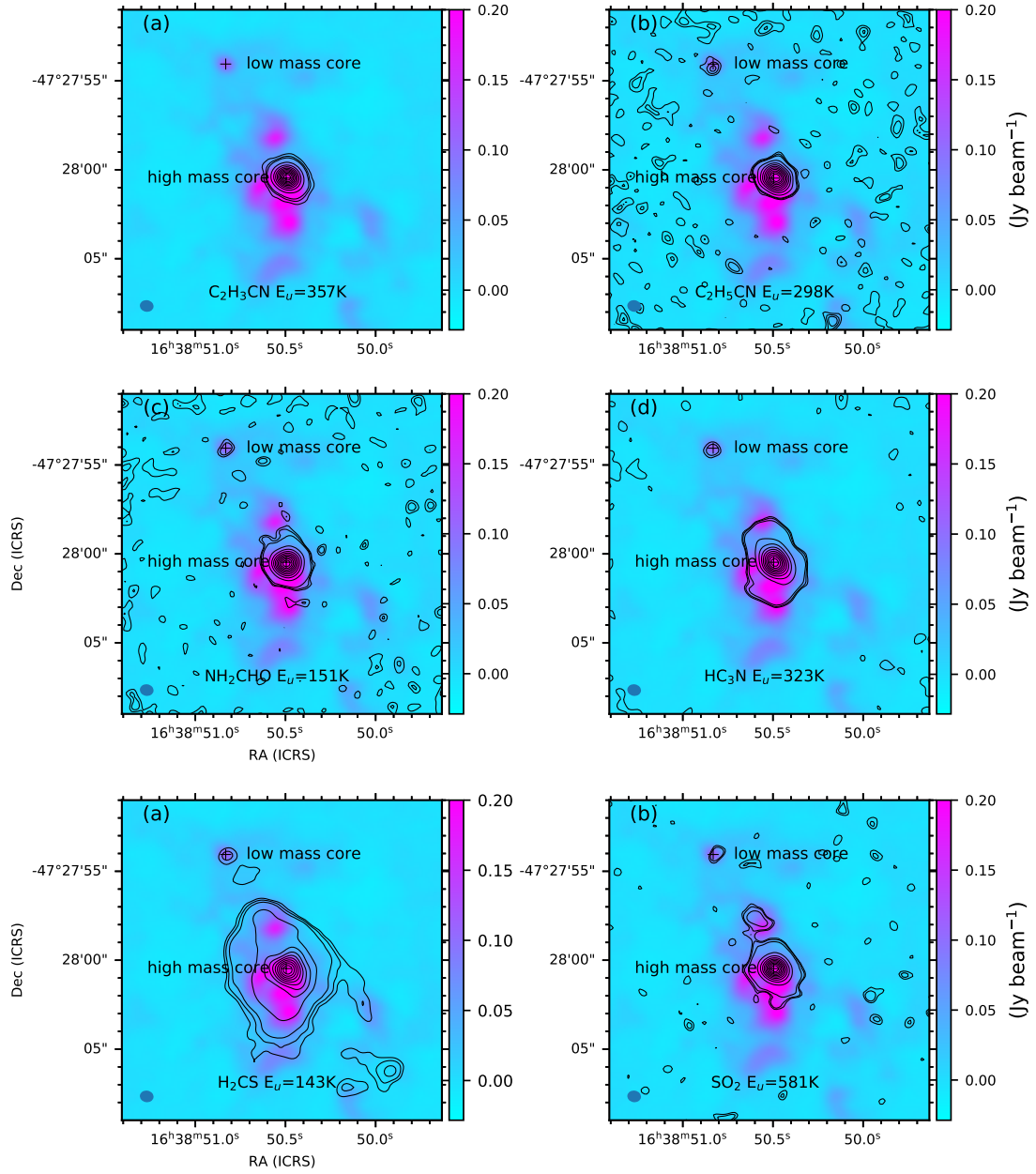


Figure 3. (continued)

Table 2. Model fitting results of the detected molecules

Name	molecule name	T_{rot} (K)	N_{tot} (cm^{-2})	$f_{\text{H}_2}^b$	$f_{\text{CH}_3\text{OH}}^c$	
Low-mass line-rich core	CH ₃ OH; E	92(6)	3.8×10^{16} (0.2)			
	CH ₃ OH; A	92(6)	2.0×10^{15} (0.2)			
	CH ₃ OH ^a	92	2.0×10^{16}	8.7×10^{-8} (0.9)	1	
	CH ₃ OCHO $v_{18}=1$	90(28)	1.1×10^{16} (0.4)	4.8×10^{-8} (2.0)	0.55(0.2)	
	CH ₃ OCHO	90(9)	1.0×10^{16} (0.1)	4.3×10^{-8} (0.4)	0.49(0.07)	
	¹³ CH ₃ OH	121(39)	8.0×10^{15} (0.4)	3.5×10^{-8} (0.2)	0.4(0.05)	
	CH ₃ OCH ₃	50(4)	7.2×10^{15} (0.1)	3.1×10^{-8} (0.06)	0.36(0.04)	
	C ₂ H ₅ OH	130(6)	3.0×10^{15} (0.6)	1.3×10^{-8} (0.3)	0.15(0.04)	
	aGg ¹ -(CH ₂ OH) ₂	66(6)	2.5×10^{15} (0.8)	1.1×10^{-8} (0.3)	0.13(0.04)	
	CH ₃ COCH ₃	93(29)	1.3×10^{15} (0.2)	5.7×10^{-9} (1.1)	0.066(0.01)	
	H ₂ CS	70(5)	8.4×10^{14} (0.6)	3.7×10^{-9} (0.3)	0.043(0.006)	
	C ₂ H ₅ CN	96(14)	5.6×10^{14} (1.1)	2.0×10^{-9} (0.4)	0.023(0.005)	
	H ₂ CCO	123(19)	4.8×10^{14} (0.8)	2.1×10^{-9} (0.4)	0.024(0.005)	
	CH ₃ CHO	93(9)	2.7×10^{14} (0.6)	1.2×10^{-9} (0.2)	0.014(0.003)	
	t-HCOOH	97(4)	1.7×10^{14} (0.1)	7.4×10^{-10} (0.4)	0.0085(0.001)	
	NH ₂ CHO	55(18)	7.0×10^{13} (0.5)	3.0×10^{-10} (0.2)	0.003(0.0003)	
	Hot core	SO ₂ $v_2=1$	198(22)	4.0×10^{17} (2.9)	2.1×10^{-6} (1.5)	1.24(0.9)
		CH ₃ OH; E	142(2)	5.0×10^{17} (0.1)		
CH ₃ OH; A		142(2)	1.5×10^{17} (0.1)			
CH ₃ OH ^a		142	3.3×10^{17}	1.7×10^{-6} (0.2)	1	
¹³ CH ₃ OH		130(37)	2.2×10^{17} (0.1)	1.2×10^{-6} (0.1)	0.71(0.1)	
CH ₃ OCHO $v_{18}=1$		170(31)	2.0×10^{17} (0.9)	1.1×10^{-6} (0.5)	0.65(0.3)	
CH ₃ OCHO		170(10)	2.0×10^{17} (0.1)	1.1×10^{-6} (0.1)	0.65(0.1)	
CH ₃ OCH ₃		93(5)	1.3×10^{17} (0.2)	6.8×10^{-7} (1.3)	0.4(0.09)	
CH ₃ COCH ₃		126(37)	1.0×10^{17} (0.9)	5.3×10^{-7} (4.8)	0.31(0.28)	
C ₂ H ₅ OH		152(19)	9.0×10^{16} (0.5)	4.7×10^{-7} (0.6)	0.28(0.05)	
C ₂ H ₅ CN		149(39)	6.5×10^{16} (0.5)	3.4×10^{-7} (0.4)	0.2(0.03)	
t-HCOOH		135(49)	3.7×10^{16} (1.5)	2.0×10^{-7} (0.8)	0.12(0.05)	
C ₂ H ₃ CN $v_{11}=1$		171(53)	3.5×10^{16} (1.0)	1.8×10^{-7} (0.5)	0.11(0.03)	
H ₂ CS		101(1)	3.0×10^{16} (0.1)	1.6×10^{-7} (0.2)	0.09(0.02)	
aGg ¹ -(CH ₂ OH) ₂		145(6)	2.4×10^{16} (1.1)	1.3×10^{-7} (0.6)	0.076(0.04)	
CH ₃ CHO		160(19)	1.5×10^{16} (0.2)	7.9×10^{-8} (1.3)	0.046(0.009)	
C ₂ H ₃ CN		171(8)	1.4×10^{16} (0.9)	7.4×10^{-8} (4.8)	0.04(0.03)	
H ₂ CCO		159(33)	1.3×10^{16} (0.5)	6.8×10^{-8} (2.7)	0.04(0.02)	
³⁴ SO ₂		134(14)	8.5×10^{15} (3.1)	4.5×10^{-8} (1.7)	0.026(0.01)	
NH ₂ CHO		150(39)	2.5×10^{15} (1.3)	1.3×10^{-8} (0.7)	0.008(0.004)	

NOTE— ^a $N_{\text{CH}_3\text{OH}} = [N_{\text{CH}_3\text{OH}; \text{E}} + N_{\text{CH}_3\text{OH}; \text{A}}]/2$, where the capital letter E and A represent different transitions.

^b $f_{\text{H}_2} = N_{\text{tot}}/N_{\text{H}_2}$, $N_{\text{H}_2} = 2.3(0.04) \times 10^{23} \text{ cm}^{-2}$ for the low-mass line-rich core and $N_{\text{H}_2} = 1.9(0.2) \times 10^{23} \text{ cm}^{-2}$ for the hot core.

^c $f_{\text{CH}_3\text{OH}} = N_{\text{tot}}/N_{\text{CH}_3\text{OH}}$.

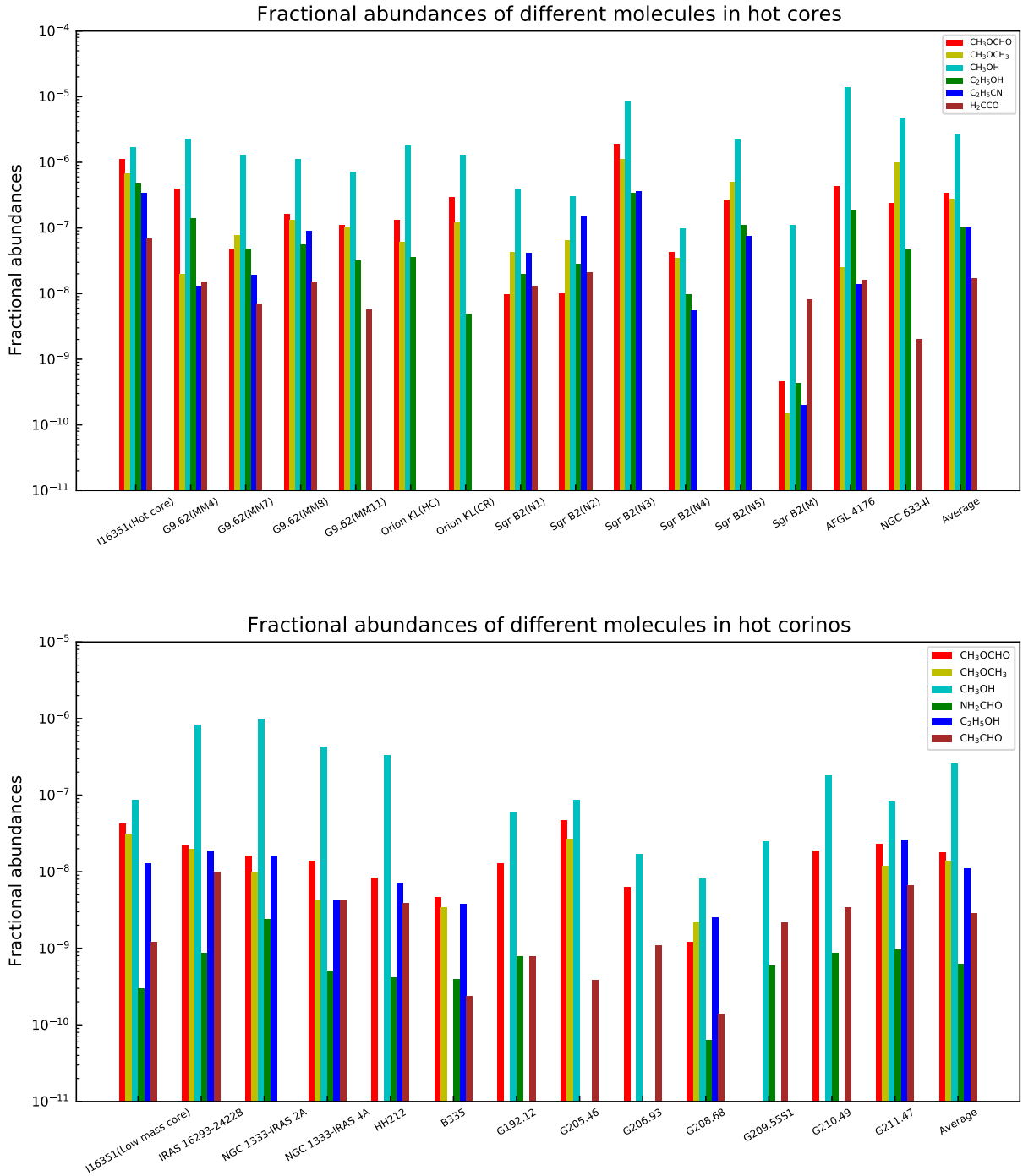


Figure 4. Fractional abundances of different molecules relative to H₂ in I16351 and the other hot cores and hot corinos listed in Table B1 and Table B2.

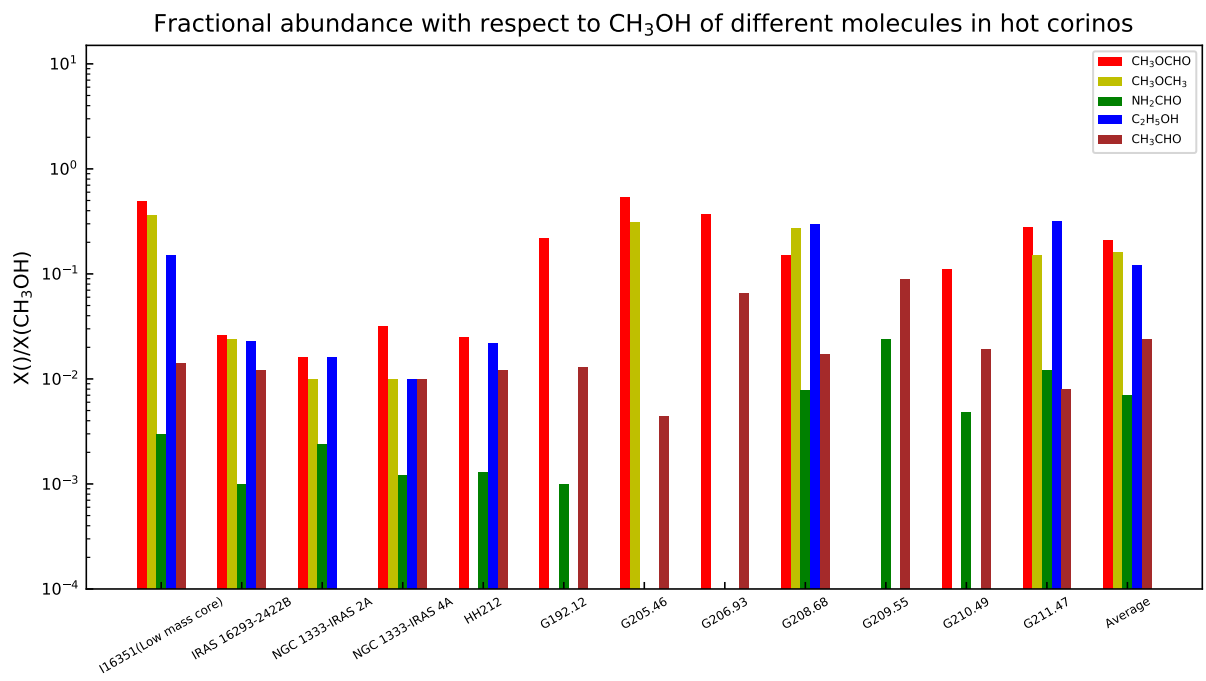


Figure 5. Fractional abundances of different molecules relative to CH₃OH in I16351 low-mass line-rich core and the other hot corinos listed in Table B2

ACKNOWLEDGMENT

This paper makes use of the following ALMA data: ADS/JAO.ALMA#2017.1.00545.S. ALMA is a partnership of ESO (representing its member states), NSF (USA), and NINS (Japan), together with NRC (Canada), MOST and ASIAA (Taiwan), and KASI (Republic of Korea), in cooperation with the Republic of Chile. The Joint ALMA Observatory is operated by ESO, AUI/NRAO, and NAOJ. This work has been supported by National Key R&D Program of China (No.2022YFA1603101), and by NSFC through the grants No.12033005, No.12073061, No.12122307, and No.12103045. S.-L. Qin thanks the Xinjiang Uygur

Autonomous Region of China for their support through the Tianchi Program. MYT acknowledges the support by NSFC through grants No.12203011, and Yunnan provincial Department of Science and Technology through grant No.202101BA070001-261. T. Zhang thanks the student’s exchange program of the Collaborative Research Centre 956, funded by the Deutsche Forschungsgemeinschaft (DFG).

Software: astropy (Astropy Collaboration et al. 2013, 2018), CASA (McMullin et al. 2007), XCLASS (Möller et al. 2017), MAGIX (Möller et al. 2013)

APPENDIX

A. FULL LINE LISTS

According to the number of identified emission lines, we arrange the order of molecules in the full list of COM transitions. The list of COM transitions used to derive rotational temperatures and column densities is shown

in Table A1. Table A1 in Appendix A shows that the transition, the rest frequencies (GHz), the upper-level energy (E_u), and the line strength (S_μ^2) of each molecular.

Table A1. Properties of Unblended Transitions

Molecular Name	Transition	Frequency (GHz)	E_u (K)	S_μ^2 (Debye ²)	Core name	Note
CH ₃ OCHO v=0	11(8,4)-10(7,4)E	342.51034	81.40352	3.46422	Hot core	
	16(13,4)-16(12,5)E	342.683424	335.27508	1.72784	Hot core	
	27(13,14)-27(12,15)E	342.69288	335.27641	5.56387	Hot core/Low-mass line-rich core	
	27(13,15)-27(12,16)A	343.72097	258.47228	5.5622	Hot core	
	27(7,20)-26(7,19)E	343.75801	258.47556	67.17309	Hot core	
	28(24,4)-27(24,3)A	343.79865	589.86175	19.94798	Hot core	
	28(23,5)-27(23,4)A	343.81403	589.85602	24.43765	Hot core	
	28(23,5)-27(23,4)E	343.826593	589.85	24.44059	Hot core	
	28(23,6)-27(23,5)E	343.835114	560.10214	24.43829	Hot core	
	28(22,6)-27(22,5)A	343.854153	560.09558	28.73324	Hot core/Low-mass line-rich core	
	28(22,6)-27(22,5)E	343.862096	560.09135	28.736	Hot core	
	28(22,7)-27(22,6)E	343.887467	531.65761	28.73425	Hot core/Low-mass line-rich core	
	28(21,8)-27(21,7)A	343.887483	531.65761	32.83771	Hot core	
	28(21,7)-27(21,6)A	343.921695	289.13552	32.8377	Hot core	
	24(13,11)-24(12,12)A	345.073057	104.42367	4.56561	Hot core	
	16(6,11)-15(5,10)A	343.958362	504.53073	2.71117	Hot core	
	28(20,8)-27(20,7)A	343.981148	504.52218	36.74693	Hot core	
	28(20,9)-27(20,8)E	343.98245	504.52325	36.74095	Hot core	
	28(20,8)-27(20,7)E	344.322992	431.08887	36.74080	Hot core	
	28(17,11)-27(17,10)A	344.349515	431.30336	47.30097	Hot core/Low-mass line-rich core	
28(17,12)-27(17,11)E	344.515454	409.2671	47.30336	Hot core/Low-mass line-rich core		
28(16,12)-27(16,11)E	344.523525	409.26331	50.42985	Hot core/Low-mass line-rich core		

Table A1 continued

Table A1 (*continued*)

Molecular Name	Transition	Frequency (GHz)	E_u (K)	S_μ^2 (Debye ²)	Core name	Note
	28(16,12)-27(16,11)E	344.541314	409.26057	50.42682	Hot core/Low-mass line-rich core	
	28(16,13)-27(16,12)E	344.783597	388.77694	50.43269	Hot core/Low-mass line-rich core	
	28(15,14)-27(15,13)E	344.957101	235.97897	53.37525	Hot core/Low-mass line-rich core	
	20(13,8)-20(12,9)A	344.957127	235.97897	3.20036	Hot core/Low-mass line-rich core	
	20(13,7)-20(12,8)A	345.132629	224.17841	3.20036	Hot core/Low-mass line-rich core	
	19(13,6)-19(12,7)A	345.132655	224.17841	2.84622	Hot core	
	19(13,7)-19(12,8)A	345.28132	212.97193	2.84622	Hot core	
	18(13,5)-18(12,6)A	345.4058639	202.35893	2.48351	Hot core	
	17(13,4)-17(12,5)A	345.6508346	80.31116	2.11147	Hot core	
	9(9,1)-8(8,1)E	345.662771	80.33274	3.89922	Hot core	
	9(9,0)-8(8,0)E	345.718662	80.31960	3.89833	Hot core	
	9(9,0)-8(8,1)A	342.342185	269.49634	3.89598	Hot core	
	30(2,28)-29(3,27)E	342.530119	269.49054	10.005	Hot core/Low-mass line-rich core	
	30(2,28)-29(3,27)A	342.35142	269.49679	10.00214	Hot core	
	30(3,28)-29(3,27)E	342.358225	269.49625	78.03662	Hot core/Low-mass line-rich core	
	30(2,28)-29(2,27)E	342.358279	269.49553	78.03333	Hot core/Low-mass line-rich core	
	31(1,30)-30(2,29)A	343.43526	257.07971	11.89421	Hot core/Low-mass line-rich core	
	28(4,24)-27(4,23)E	343.443944	257.0807	71.57138	Hot core/Low-mass line-rich core	
	28(4,24)-27(4,23)A	343.541355	303.90939	71.58443	Hot core	
	25(13,13)-25(12,14)E	343.56185	303.91699	4.90072	Hot core	
	25(13,12)-25(12,13)A	343.561883	303.91699	4.89913	Hot core	
	25(13,13)-25(12,14)A	344.051371	478.72469	4.89913	Hot core/Low-mass line-rich core	
	28(19,9)-27(19,8)A	344.335357	431.08400	40.45991	Hot core/Low-mass line-rich core	
	28(17,11)-27(17,10)E	344.759096	388.78295	47.29676	Hot core/Low-mass line-rich core	*
	28(15,13)-27(15,12)A	344.02926	276.09723	53.37173	Hot core/Low-mass line-rich core	
	32(1,32)-31(1,31)E	345.067795	369.64085	88.1756	Hot core/Low-mass line-rich core	
	28(14,14)-27(14,13)E	345.069059	369.64307	56.11927	Hot core/Low-mass line-rich core	
	28(14,15)-27(14,14)A	345.091465	369.63767	56.11927	Hot core/Low-mass line-rich core	
	28(14,15)-27(14,14)E	345.466962	351.85611	56.12379	Hot core/Low-mass line-rich core	
	28(13,16)-27(13,15)A	345.486602	351.85130	58.67428	Hot core/Low-mass line-rich core	
	28(13,16)-27(13,15)E	345.974664	335.43319	58.68009	Hot core/Low-mass line-rich core	
	28(12,16)-27(12,15)E	345.985381	335.43442	61.03512	Hot core/Low-mass line-rich core	
	28(12,17)-27(12,16)A	346.001616	335.43002	61.04559	Hot core/Low-mass line-rich core	
CH ₃ COCH ₃ v=0	17(17,1)-16(16,1)EA	342.4106413	146.85179	552.43037	Hot core	
	40(2,39)-40(0,40)EA	342.4856638	411.39562	41.07562	Hot core	
	17(17,0)-16(16,0)EE	342.485233	147.06155	2209.9853	Hot core	
	18(14,4)-17(13,5)EA	342.596906	147.13957	3.20786	Hot core	
	17(17,1)-16(16,1)EE	342.5948875	146.9497	2210.2712	Hot core	
	17(17,1)-16(16,0)AA	342.7800345	147.04764	828.91802	Hot core	
	31(4,27)-30(5,26)EA	343.338875	288.65894	881.61793	Hot core	
	31(5,27)-30(4,26)EE	343.386	288.63372	3176.311	Hot core	
	31(5,27)-30(4,26)AA	343.43308	288.60878	1322.10583	Hot core	
	37(27,10)-37(24,13)AA	344.46661	593.90913	21.18788	Hot core	
	21(9,12)-21(6,15)AA	343.4435689	174.6791	0.94626	Hot core/Low-mass line-rich core	
	32(4,29)-31(3,28)AA	344.549874	293.69203	2389.27358	Hot core/Low-mass line-rich core	
	33(2,31)-32(3,30)EE	345.639619	298.03287	592.06425	Hot core/Low-mass line-rich core	*

Table A1 *continued*

Table A1 (*continued*)

Molecular Name	Transition	Frequency (GHz)	E_u (K)	S_μ^2 (Debye ²)	Core name	Note
	15(7,8)-14(6,9)EE	345.6739538	92.93574	115.73717	Hot core/Low-mass line-rich core	
³⁴ SO ₂ v=0	8(4,4)-8(3,5)	345.1686641	71.047	9.76929	Hot core	
	9(4,6)-9(3,7)	345.2856199	79.31737	11.41398	Hot core	
	9(4,6)-9(3,7)	345.2856217	79.31737	11.41398	Hot core	
	6(4,2)-6(3,3)	345.5530927	57.26899	6.34216	Hot core	
	5(4,2)-5(3,3)	345.6512934	51.76028	4.49068	Hot core	
	4(4,0)-4(3,1)	345.6787871	47.1706	2.44173	Hot core	
	17(4,14)-17(3,15)	345.929349	178.77039	24.49458	Hot core	
	19(1,19)-18(0,18)	344.5810445	167.65667	42.23967	Hot core	
	13(4,10)-13(3,11)	344.8079147	121.63281	17.92316	Hot core	
	15(4,12)-15(3,13)	344.9875847	148.34497	21.20438	Hot core	
	11(4,8)-11(3,9)	344.9981602	98.62644	14.6664	Hot core	
7(4,4)-7(3,5)	345.5196563	63.69764	8.08591	Hot core		
aGg'-(CH ₂ OH) ₂ v=0	34(14,21)v=0-33(14,20)v=1	342.5799012	388.78369	1085.335	Hot core/Low-mass line-rich core	
	34(4,31)v=1-33(4,30)v=0	342.80051910	297.12558	990.16715	Hot core/Low-mass line-rich core	
	34(3,31)v=1-33(3,30)v=0	342.850907	297.12209	1298.895	Hot core/Low-mass line-rich core	
	27(6,22)v=1-26(5,21)v=1	343.0017164	205.05936	47.55677	Hot core/Low-mass line-rich core	
	34(11,23)v=0-33(11,22)v=1	343.9543754	352.45528	909.59335	Hot core/Low-mass line-rich core	
	37(0,37)-v=1-36(0,36)v=1	343.997789	286.70541	317.01833	Hot core/Low-mass line-rich core	
	57(18,40)v=0-57(17,40)v=1	344.612515	971.39018	35.08034	Hot core/Low-mass line-rich core	
	33(6,27)v=0-32(6,26)v=1	344.8010266	299.19716	1243.89335	Hot core/Low-mass line-rich core	
	35(5,31) v=0-34(5,30)v=1	344.9464396	321.67857	1085.81788	Hot core	
	33(11,22)v=1-32(11,21)v=0	345.7384426	335.94816	878.0009	Hot core	
C ₂ H ₅ OH v=0	17(2,15)-17(1,17),g-	344.9501561	196.49691	0.31550	Hot core/Low-mass line-rich core	
	7(7,1)-6(6,1),g+	345.17394930	139.90163	7.89577	Hot core/Low-mass line-rich core	
	21(1,21)-20(1,20),g+	345.2292848	241.5535	33.33569	Hot core/Low-mass line-rich core	
	21(1,21)-20(1,20),g-	345.2953553	246.22196	32.93056	Hot core/Low-mass line-rich core	
	21(0,21)-20(0,20),g-	345.4081651	246.20853	32.93167	Hot core/Low-mass line-rich core	
	20(3,18)-19(3,17),g+	345.6485708	242.48944	32.28459	Hot core/Low-mass line-rich core	
	20(3,18)-19(3,17),g-	345.6566222	347.2135	29.93737	Hot core/Low-mass line-rich core	
	20(11,9)-19(11,8),g-	346.0172119	384.56138	21.63848	Hot core/Low-mass line-rich core	
C ₂ H ₅ CN v=0	43(8,35)-43(7,36)	342.622337	478.06113	34.90162	Hot core	
	15(5,11)-14(4,10)	342.6518898	79.39247	9.20326	Hot core/Low-mass line-rich core	
	15(5,10)-14(4,11)	342.6775645	79.39255	9.20398	Hot core/Low-mass line-rich core	
	38(5,33)-37(5,32)	343.194574	347.4118	553.52713	Hot core/Low-mass line-rich core	
	10(6,5)-9(5,4)	344.27894	63.66672	8.97431	Hot core/Low-mass line-rich core	
	39(3,37)-38(3,36)	345.921198	344.45762	573.18734	Hot core/Low-mass line-rich core	
	32(8,25)-32(7,26)	345.93802	298.17246	24.57802	Hot core/Low-mass line-rich core	*
H ₂ CS v=0	10(0,10)-9(0,9)	342.9464239	90.59115	27.19603	Hot core/Low-mass line-rich core	
	10(5,5)-9(5,4)	343.202331	417.55066	61.03878	Hot core/Low-mass line-rich core	
	10(4,7)-9(4,6)	343.3085	300.5408	22.78476	Hot core/Low-mass line-rich core	
	10(2,9)-9(2,8)	343.3220819	143.34223	26.04309	Hot core/Low-mass line-rich core	
	10(3,8)-9(3,7)	343.4099625	209.01721	74.06191	Hot core/Low-mass line-rich core	
	10(2,8)-9(2,7)	343.813168	143.37729	26.10949	Hot core/Low-mass line-rich core	*
CH ₃ OCHO v ₁₈ =1	28(10,19)-27(10,18)A	344.420363	492.85974	65.12347	Hot core/Low-mass line-rich core	
	28(6,23)-27(6,22)A	345.148	451.66286	70.83473	Hot core/Low-mass line-rich core	

Table A1 (*continued*)

Table A1 (*continued*)

Molecular Name	Transition	Frequency (GHz)	E_u (K)	S_μ^2 (Debye ²)	Core name	Note
	28(9,20)-27(9,19)A	345.510	480.50639	66.90806	Hot core/Low-mass line-rich core	
	28(12,17)-27(12,16)A	343.134119	521.89351	60.99147	Hot core/Low-mass line-rich core	
	28(11,17)-27(11,16)A	343.66346	506.66854	63.1497	Hot core/Low-mass line-rich core	
CH ₃ OCH ₃ v=0	19(0,19)-18(1,18)AE	342.60806	167.141	130.68396	Hot core/Low-mass line-rich core	
	17(2,16)-16(1,15)EA	343.753306	143.69799	45.93527	Hot core/Low-mass line-rich core	
	19(1,19)-18(0,18)EA	344.357816	167.17839	55.06275	Hot core/Low-mass line-rich core	
	38(4,35)-38(5,34)EA	344.35804	697.06888	257.36625	Hot core	
	11(3,9)-10(2,8)AA	344.518594	72.78343	29.84891	Hot core/Low-mass line-rich core	
CH ₃ OH v=0	13(1,12)-13(0,13)-,vt=0	342.72983	227.4725	24.37811	Hot core/Low-mass line-rich core	
	18(2,16)-17(3,14)-,vt=0	344.109132	419.39854	5.31374	Hot core	
	18(3,15)-17(4,14)E,vt=0	345.91926	459.43023	22.4084	Hot core/Low-mass line-rich core	*
	16(1,15)-15(2,14)A,vt=0	345.903916	332.6488	28.51774	Hot core/Low-mass line-rich core	
	19(1,19)-18(2,16)A,vt=0	344.443433	451.22691	23.97181	Hot core/Low-mass line-rich core	
H ₂ CCO v=0	17(0,17)-16(0,16)	343.17257	148.30454	34.27746	Hot core/Low-mass line-rich core	
	17(4,14)-16(4,13)	343.2504	356.83923	32.38127	Hot core/Low-mass line-rich core	
	17(2,16)-16(2,15)	343.376133	200.53312	33.8061	Hot core/Low-mass line-rich core	
	17(3,15)-16(3,14)	343.384676	265.71292	99.63928	Hot core/Low-mass line-rich core	
	17(2,15)-16(2,14)	343.693935	200.60564	33.80534	Hot core/Low-mass line-rich core	
¹³ CH ₃ OH v=0	8(-3,6)-9(-2,8)	344.040629	144.4915	2.17479	Hot core/Low-mass line-rich core	*
	3(3,0)-4(2,2)	344.671733	61.55273	0.24805	Hot core	
	2(2,0)-3(1,3)++	345.083793	44.59627	0.30348	Hot core	
	4(0,4)-3(-1,3)	345.132599	35.76015	1.54925	Hot core/Low-mass line-rich core	
NH ₂ CHO v=0	16(3,13)-15(3,12)	343.083117	165.99525	201.84690	Hot core/Low-mass line-rich core	
	17(1,17)-16(1,16)	343.1969863	151.99629	221.24033	Hot core/Low-mass line-rich core	
	17(0,17)-16(0,16)	345.181258	151.58895	221.41017	Hot core/Low-mass line-rich core	*
	16(1,15)-15(1,14)	345.3253906	145.15586	207.83422	Hot core/Low-mass line-rich core	
C ₂ H ₃ CN v=0	36(5,31)-35(5,30)	342.3755639	357.69133	1541.37365	Hot core	*
	15(6,9)-16(5,12)	342.5893637	132.43412	4.12349	Hot core	
	36(4,32)-35(4,31)	343.4465355	338.62854	1552.2491	Hot core	
t-HCOOH v=0	16(1,16)-15(1,15)	342.521194	143.59095	32.16799	Hot core/Low-mass line-rich core	
	15(1,14)-14(1,13)	343.952343	136.28091	30.10023	Hot core/Low-mass line-rich core	
	16(0,16)-15(0,15)	345.030561	143.05228	31.05632	Hot core	*
CH ₃ C ₃ N v=0	83(2)-82(2)	342.6855194	720.90534	3742.49011	Low-mass line-rich core	
	83(0)-82(0)	342.6984005	690.98043	3745.47430	Low-mass line-rich core	
	83(3)-82(3)	342.6694207	758.3055	7480.735	Low-mass line-rich core	
CH ₃ SH v ₁₂ =1	16(-1,16)A,vt=1	344.40893	480.43037	2.96268	Low-mass line-rich core	
	2(-2,1)-1(-1,1)E,vt=1	344.87788	325.75082	0.65398	Low-mass line-rich core	
	15(1,14)-14(0,14)E,vt=1	345.336513	427.10456	2.5329	Low-mass line-rich core	
c-H ₂ C ₃ O v=0	27(1,27)-26(1,26)	345.389613	235.83485	1554.06816	Low-mass line-rich core	
	26(1,25)-25(1,24)	345.6303058	233.86764	1483.9321	Low-mass line-rich core	
SO ₂ v ₂ =1	23(3,21)-23(2,22)	342.4359377	1040.88125	29.57632	Hot core	
	24(2,22)-23(3,21)	343.9237569	1057.70354	19.5591	Hot core	
C ₂ H ₃ CN v ₁₁ =1	36(7,29)-35(7,28),F=37-36	342.928828	737.05933	511.8907	Hot core	
	36(4,33)-35(4,32),F=35-34	343.639977	667.27558	525.44888	Hot core	
CH ₃ CHO v=0	30(2,28)-29(3,27)A, vt=2	343.830738	827.3158	22.24928	Hot core/Low-mass line-rich core	
	18(2,17)-17(2,16)A,vt=1	343.8330821	371.84089	225.86166	Hot core/Low-mass line-rich core	*

Table A1 *continued*

Table A1 (*continued*)

Molecular Name	Transition	Frequency (GHz)	E_u (K)	S_μ^2 (Debye ²)	Core name	Note
CH ₃ C ₄ H v=0	85(2)-84(2)	354.8511129	781.44479	266.59178	Hot core	
	85(4)-84(4)	345.8116518	876.34192	270.22466	Hot core	
HC ₅ N v=0	J=129-128	343.2256445	1071.10155	7255.3324	Hot core/Low-mass line-rich core	
SiC ₄ v=0	112-111	343.237469	931.14787	4445.08234	Hot core	
t-HCOOD v=0	40(5,35)-40(4,36)	343.97053	939.40848	2.14618	Hot core	
CH ₃ OH v ₁₂ =1	10(2,9)-11(3,9)E,vt=1	344.312267	491.90986	31.24862	Hot core/Low-mass line-rich core	
SO ₂ v=0	34(3,31)-34(2,32)	342.7616232	581.91876	50.73556	Hot core/Low-mass line-rich core	*
CS v=0	7-6	342.88285	65.8273	26.75185	Hot core/Low-mass line-rich core	
c-C ₂ H ₄ O v=0	9(5,5)-8(4,4)	345.68832	90.40751	66.52984	Hot core	
HNCCC v=0	J=37-36, F=36-37	345.343	314.95191	0.86737	Low-mass line-rich core	
HC ₃ N v=0	J=38-37	345.60901	323.49156	529.12907	Hot core/Low-mass line-rich core	*
NS v=0	J=15/2-13/2,Ω=1/2	345.823288	70.79666	24.02695	Hot core/Low-mass line-rich core	
	F=17/2-15/2,l=e					

NOTE—The rows marked with * indicate that the transitions of the molecules are used for Figure 3.

B. FRACTIONAL ABUNDANCE LISTS

The fractional abundances of hot cores and hot corinos from other sources reported in literature are listed in Tables B1 and B2.

Table B1. Molecular abundances with respect to H₂ in I16351 hot core and other sources.

Hot core	CH ₃ OH	CH ₃ OCH ₃	CH ₃ OCHO	C ₂ H ₅ OH	C ₂ H ₅ CN	H ₂ CCO	Reference
	/[H ₂]	/[H ₂]	/[H ₂]	/[H ₂]	/[H ₂]	/[H ₂]	
Hot core	1.7(-6)	6.8(-7)	1.1(-6)	4.7(-7)	3.4(-7)	6.8(-8)	this work
G9.62+0.19(MM4)	2.3(-6)	2.0(-7)	3.9(-7)	1.4(-7)	1.3(-8)	1.5(-8)	1
G9.62+0.19(MM7)	1.3(-6)	7.8(-8)	4.8(-8)	4.8(-8)	1.9(-8)	7.0(-9)	1
G9.62+0.19(MM8)	1.1(-6)	1.3(-7)	1.6(-7)	5.5(-8)	9.0(-8)	1.5(-8)	1
G9.62+0.19(MM11)	7.1(-7)	1.0(-7)	1.1(-7)	3.2(-8)	-	5.7(-9)	1
Orion KL(HC)	1.8(-6)	6.1(-8)	1.3(-7)	3.6(-8)	-	-	2
Orion KL(CR)	1.3(-6)	1.2(-7)	2.9(-7)	4.9(-9)	-	-	2
Sgr B2(N1)	3.9(-7)	4.3(-8)	9.6(-9)	2.0(-8)	4.1(-8)	1.3(-8)	3
Sgr B2(N2)	3.0(-7)	6.5(-8)	1.0(-8)	2.8(-8)	1.5(-7)	2.1(-8)	3
Sgr B2(N3)	8.3(-6)	1.1(-6)	1.9(-6)	3.4(-7)	3.6(-7)	-	4
Sgr B2(N4)	9.8(-8)	3.5(-8)	4.3(-8)	9.8(-9)	5.5(-9)	-	4
Sgr B2(N5)	2.2(-6)	5.0(-7)	2.7(-7)	1.1(-7)	7.6(-8)	-	4
Sgr B2(M)	1.1(-7)	1.5(-10)	4.6(-10)	4.3(-10)	2.0(-10)	8.0(-9)	3
AFGL 4176	1.4(-5)	2.5(-8)	4.3(-7)	1.9(-7)	1.4(-8)	1.6(-8)	5
NGC 6334I	4.7(-6)	1.0(-6)	2.4(-7)	4.7(-8)	-	2.0(-9)	6
Average	2.7(-6)	2.8(-7)	3.4(-7)	1.0(-7)	1.0(-7)	1.7(-8)	

NOTE—A(B)=A×10^B. 1. (Peng et al. 2022). 2.(Tercero et al. 2018). 3. (Belloche et al. 2013). 4. (Bonfand et al. 2019). 5. (Bøgelund et al. 2019). 6. (Zernickel et al. 2012).

Table B2. Molecular abundances with respect to H₂ and CH₃OH in I16351 hot corino and other sources.

Hot corino	CH ₃ OH		CH ₃ OCH ₃		CH ₃ OCHO		C ₂ H ₅ OH		NH ₂ CHO		CH ₃ CHO		Reference
	/[CH ₃ OH]	/[H ₂]	/[CH ₃ OH]	/[H ₂]	/[CH ₃ OH]	/[H ₂]	/[CH ₃ OH]	/[H ₂]	/[CH ₃ OH]	/[H ₂]	/[CH ₃ OH]	/[H ₂]	
Low-mass core	1	8.7(-8)	3.6(-1)	3.1(-8)	4.9(-1)	4.3(-8)	1.5(-1)	1.3(-8)	3.0(-3)	3.0(-10)	1.4(-2)	1.2(-9)	this work
IRAS 16293-2422B	1	8.3(-7)	2.4(-2)	2.0(-8)	2.6(-2)	2.2(-8)	2.3(-2)	1.9(-8)	1.0(-3)	8.7(-10)	1.2(-2)	1.0(-8)	1,2,3,8
NGC 1333-IRAS 2A	1	1.0(-6)	1.0(-2)	1.0(-8)	1.6(-2)	1.6(-8)	1.6(-2)	1.6(-8)	2.4(-3)	2.4(-9)	-	-	4
NGC 1333-IRAS 4A	1	4.3(-7)	1.0(-2)	4.3(-9)	3.2(-2)	1.4(-8)	1.0(-2)	4.3(-9)	1.2(-3)	5.1(-10)	1.0(-2)	4.3(-9)	4,9
HH212	1	3.3(-7)	-	-	2.5(-2)	8.4(-9)	2.2(-2)	7.1(-9)	1.3(-3)	4.2(-10)	1.2(-2)	3.9(-9)	5
B335	-	-	-	3.4(-9)	-	4.6(-9)	-	3.8(-9)	-	4.0(-10)	-	2.4(-10)	6
G192.12-11.10	1	6.0(-8)	-	-	2.2(-1)	1.3(-8)	-	-	1.3(-2)	7.9(-10)	1.3(-2)	7.9(-10)	7
G205.46-14.56S1-A	1	8.7(-8)	3.1(-1)	2.7(-8)	5.4(-1)	4.7(-8)	-	-	-	-	4.4(-3)	3.9(-10)	7
G206.93-16.61W2	1	1.7(-8)	-	-	3.7(-1)	6.3(-9)	-	-	-	-	6.5(-2)	1.1(-9)	7
G208.68-19.20N1	1	8.2(-9)	2.7(-1)	2.2(-9)	1.5(-1)	1.2(-9)	3.0(-1)	2.5(-9)	7.8(-3)	6.4(-11)	1.7(-2)	1.4(-10)	7
G209.55-19.68S1	1	2.5(-8)	-	-	-	-	-	-	2.4(-2)	6.0(-10)	8.8(-2)	2.2(-9)	7
G210.49-19.79W-A	1	1.8(-7)	-	-	1.1(-1)	1.9(-8)	-	-	4.8(-3)	8.6(-10)	1.9(-2)	3.4(-9)	7
G211.47-19.27S	1	8.2(-8)	1.5(-1)	1.2(-8)	2.8(-1)	2.3(-8)	3.2(-1)	2.6(-8)	1.2(-2)	9.7(-10)	8.0(-3)	6.6(-9)	7
Average	1	2.6(-7)	1.6(-1)	1.4(-8)	2.1(-1)	1.8(-8)	1.2(-1)	1.1(-8)	7.0(-3)	6.3(-10)	2.4(-2)	2.9(-9)	

NOTE—A(B)=A×10^B. 1.(Jørgensen et al. 2018). 2.(Jørgensen et al. 2020). 3.(Drozdovskaya et al. 2019). 4.(Taquet et al. 2015). 5.(Lee et al. 2017, 2019). 6.(Imai et al. 2016). 7.(Hsu et al. 2022). 8.(Coutens et al. 2016). 9.(López-Sepulcre et al. 2017)

REFERENCES

- Ahmadi, A., Beuther, H., Mottram, J. C., et al. 2018, *A&A*, 618, A46, doi: [10.1051/0004-6361/201732548](https://doi.org/10.1051/0004-6361/201732548)
- Arce, H. G., Santiago-García, J., Jørgensen, J. K., Tafalla, M., & Bachiller, R. 2008, *ApJL*, 681, L21, doi: [10.1086/590110](https://doi.org/10.1086/590110)
- Astropy Collaboration, Robitaille, T. P., Tollerud, E. J., et al. 2013, *A&A*, 558, A33, doi: [10.1051/0004-6361/201322068](https://doi.org/10.1051/0004-6361/201322068)
- Astropy Collaboration, Price-Whelan, A. M., Sipőcz, B. M., et al. 2018, *ApJ*, 156, 123, doi: [10.3847/1538-3881/aabc4f](https://doi.org/10.3847/1538-3881/aabc4f)
- Baug, T., Wang, K., Liu, T., et al. 2021, *MNRAS*, 507, 4316, doi: [10.1093/mnras/stab1902](https://doi.org/10.1093/mnras/stab1902)
- Belloche, A., Garrod, R. T., Müller, H. S. P., et al. 2019, *A&A*, 628, A10, doi: [10.1051/0004-6361/201935428](https://doi.org/10.1051/0004-6361/201935428)
- Belloche, A., Müller, H. S. P., Garrod, R. T., & Menten, K. M. 2016, *A&A*, 587, A91, doi: [10.1051/0004-6361/201527268](https://doi.org/10.1051/0004-6361/201527268)
- Belloche, A., Müller, H. S. P., Menten, K. M., Schilke, P., & Comito, C. 2013, *A&A*, 559, A47, doi: [10.1051/0004-6361/201321096](https://doi.org/10.1051/0004-6361/201321096)
- Belloche, A., Maury, A. J., Maret, S., et al. 2020, *A&A*, 635, doi: [10.48550/arXiv.2002.00592](https://doi.org/10.48550/arXiv.2002.00592)
- Beuther, H., Zhang, Q., Sridharan, T. K., & Chen, Y. 2005, *ApJ*, 628, 800, doi: [10.1086/431277](https://doi.org/10.1086/431277)
- Bonfand, M., Belloche, A., Garrod, R. T., et al. 2019, *A&A*, 628, A27, doi: [10.1051/0004-6361/201935523](https://doi.org/10.1051/0004-6361/201935523)
- Bonfand, M., Belloche, A., Menten, K. M., Garrod, R. T., & Müller, H. S. P. 2017, *A&A*, 604, A60, doi: [10.1051/0004-6361/201730648](https://doi.org/10.1051/0004-6361/201730648)
- Bøgelund, E. G., Barr, A. G., Taquet, V., et al. 2019, *A&A*, 628, A2, doi: [10.1051/0004-6361/201834527](https://doi.org/10.1051/0004-6361/201834527)
- Ceccarelli, C. 2004, *The Hot Corinos of Solar Type Protostars*, 3rd edn. (Astronomical Society of the Pacific)
- Coutens, A., Jørgensen, J. K., van der Wiel, M. H. D., et al. 2016, *A&A*, 590, L6, doi: [10.48550/arXiv.1605.02562](https://doi.org/10.48550/arXiv.1605.02562)
- Csengeri, T., Belloche, A., Bontemps, S., et al. 2019, *A&A*, 632, A57, doi: [10.1051/0004-6361/201935226](https://doi.org/10.1051/0004-6361/201935226)
- Drozdovskaya, M. N., van Dishoeck, E. F., Rubin, M., Jørgensen, J. K., & Altwegg, K. 2019, *MNRAS*, 490, doi: [10.1093/mnras/stz2430](https://doi.org/10.1093/mnras/stz2430)
- Frau, P., Girart, J. M., Beltrán, M. T., et al. 2010, *ApJ*, 723, 1665, doi: [10.1088/0004-637X/723/2/1665](https://doi.org/10.1088/0004-637X/723/2/1665)
- Garrod, R. T. 2013, *ApJ*, 765, doi: [10.48550/arXiv.1302.0688](https://doi.org/10.48550/arXiv.1302.0688)
- Gieser, C., Beuther, H., Semenov, D., et al. 2021, *A&A*, 648, A66, doi: [10.1051/0004-6361/202039670](https://doi.org/10.1051/0004-6361/202039670)
- Guzmán, A. E., Guzmán, V. V., Garay, G., Bronfman, L., & Hechenleitner, F. 2018, *ApJS*, 236, 45, doi: [10.3847/1538-4365/aac01d](https://doi.org/10.3847/1538-4365/aac01d)
- Herbst, E., & van Dishoeck, E. F. 2009, *ARA&A*, 47, 427, doi: [10.1146/annurev-astro-082708-101654](https://doi.org/10.1146/annurev-astro-082708-101654)
- Hernández-Hernández, V., Zapata, L., Kurtz, S., & Garay, G. 2014, *ApJ*, 786, 38, doi: [10.1088/0004-637X/786/1/38](https://doi.org/10.1088/0004-637X/786/1/38)
- Hildebrand, R. H. 1983, *QJRAS*, 24
- Hsu, S.-Y., Liu, S.-Y., & Liu, T. 2020, *ApJ*, 898, doi: [10.48550/arXiv.2006.15850](https://doi.org/10.48550/arXiv.2006.15850)
- Hsu, S.-Y., Liu, S.-Y., Liu, T., et al. 2022, *ApJ*, 927, doi: [10.48550/arXiv.2201.02497](https://doi.org/10.48550/arXiv.2201.02497)
- Imai, M., Sakai, N., Oya, Y., et al. 2016, *ApJ*, 830, doi: [10.48550/arXiv.1610.03942](https://doi.org/10.48550/arXiv.1610.03942)
- Jørgensen, J. K., Belloche, A., & Garrod, R. T. 2020, *A&A*, 58, doi: [10.1146/annurev-astro-032620-021927](https://doi.org/10.1146/annurev-astro-032620-021927)
- Jørgensen, J. K., Müller, H. S. P., Calcutt, H., et al. 2018, *A&A*, 620, doi: [10.48550/arXiv.1808.08753](https://doi.org/10.48550/arXiv.1808.08753)
- Kauffmann, J., Bertoldi, F., Bourke, T. L., Evans, N. J., & Lee, C. W. 2008, *A&A*, 487, doi: [arXiv:0805.4205](https://doi.org/10.48550/arXiv.0805.4205)
- Kurtz, S., Cesaroni, R., Churchwell, E., Hofner, P., & Walmsley, C. M. 2000, *Hot Molecular Cores and the Earliest Phases of High-Mass Star Formation*, 3rd edn. (Protostars and Planets IV)
- Law, C. J., Zhang, Q., Öberg, K. I., et al. 2021, *ApJ*, 909, 33, doi: [10.3847/1538-4357/abdeb8](https://doi.org/10.3847/1538-4357/abdeb8)
- Lee, C.-F., Li, Z.-Y., Ho, P. T. P., et al. 2017, *ApJ*, 843, 27, doi: [10.3847/1538-4357/aa7757](https://doi.org/10.3847/1538-4357/aa7757)
- Lee, C.-F., Kwon, W., Jhan, K.-S., et al. 2019, *ApJ*, 879, doi: [10.48550/arXiv.1905.09417](https://doi.org/10.48550/arXiv.1905.09417)
- Lefloch, B., Ceccarelli, C., Codella, C., et al. 2017, *MNRAS*, 469, L73, doi: [10.1093/mnrasl/slx050](https://doi.org/10.1093/mnrasl/slx050)
- Ligterink, N. F. W., El-Abd, S. J., Brogan, C. L., et al. 2020, *ApJ*, 901, 37, doi: [10.3847/1538-4357/abad38](https://doi.org/10.3847/1538-4357/abad38)
- Liu, S.-Y., Girart, J. M., Remijan, A., & Snyder, L. E. 2002, *ApJ*, 576, 255, doi: [10.1086/341620](https://doi.org/10.1086/341620)
- Liu, T., Evans, N. J., Kim, K.-T., et al. 2020, *MNRAS*, 496, doi: [10.48550/arXiv.2006.01549](https://doi.org/10.48550/arXiv.2006.01549)
- López-Sepulcre, A., Jaber, A. A., Mendoza, E., et al. 2015, *MNRAS*, 449, 2438, doi: [10.1093/mnras/stv377](https://doi.org/10.1093/mnras/stv377)
- López-Sepulcre, A., Balucani, N., Ceccarelli, C., et al. 2019, *Interstellar Formamide (NH₂CHO), a Key Prebiotic Precursor*, 3rd edn. (ACS Earth and Space Chemistry)
- López-Sepulcre, A., Sakai, N., Neri, R., et al. 2017, *A&A*, 606, 121L, doi: [10.48550/arXiv.1707.03745](https://doi.org/10.48550/arXiv.1707.03745)
- McMullin, J. P., Waters, B., Schiebel, D., Young, W., & Golap, K. 2007, in *Astronomical Society of the Pacific Conference Series*, Vol. 376, *Astronomical Data Analysis Software and Systems XVI*, ed. R. A. Shaw, F. Hill, & D. J. Bell, 127
- Mottram, J. C., Beuther, H., Ahmadi, A., et al. 2020, *A&A*, 636, A118, doi: [10.1051/0004-6361/201834152](https://doi.org/10.1051/0004-6361/201834152)

- Möller, T., Bernst, I., Panoglou, D., et al. 2013, *A&A*, 549, A21, doi: [10.1051/0004-6361/201220063](https://doi.org/10.1051/0004-6361/201220063)
- Möller, T., Endres, C., & Schilke, P. 2017, *A&A*, 598, 7M, doi: [10.1051/0004-6361/201527203](https://doi.org/10.1051/0004-6361/201527203)
- Müller, P., H. S., Schlöder, F., Stutzki, J., & Winnewisser, G. 2005, in *j.molstruc*, 215–227, doi: [10.1016/j.molstruc.2005.01.027](https://doi.org/10.1016/j.molstruc.2005.01.027)
- Ossenkopf, V., & Henning, T. 1994, *A&A*, 291, 943
- Pagani, L., Bergin, E., Goldsmith, P. F., et al. 2019, *A&A*, 624, 5P, doi: [10.1051/0004-6361/201935267](https://doi.org/10.1051/0004-6361/201935267)
- Pagani, L., Favre, C., Goldsmith, P. F., et al. 2017, *A&A*, 604, A32, doi: [10.1051/0004-6361/201730466](https://doi.org/10.1051/0004-6361/201730466)
- Peng, Y.-p., Liu, T., Qin, S.-L., et al. 2022, *MNRAS*, 512, 4419, doi: [10.1093/mnras/stac624](https://doi.org/10.1093/mnras/stac624)
- Pickett, H. M., Poynter, R. L., Cohen, E. A., et al. 1998, in *JQSRT*, 883–890
- Qin, S.-L., Schilke, P., Wu, J., et al. 2015, *ApJ*, 803, 12, doi: [10.1088/0004-637X/803/1/39](https://doi.org/10.1088/0004-637X/803/1/39)
- Qin, S.-L., Wu, Y., Huang, M., et al. 2010, *ApJ*, 711, 399, doi: [10.1088/0004-637X/711/1/399](https://doi.org/10.1088/0004-637X/711/1/399)
- Qin, S.-L., Liu, T., Liu, X., et al. 2022, *MNRAS*, 511, 3463, doi: [10.1093/mnras/stac219](https://doi.org/10.1093/mnras/stac219)
- Remijan, A., Shiao, Y. S., Friedel, D. N., Meier, D. S., & Snyder, L. E. 2004, *ApJ*, 617, 384, doi: [10.1086/425266](https://doi.org/10.1086/425266)
- Rivilla, V. M., Beltrán, M. T., Cesaroni, R., et al. 2017, *A&A*, 598, 22, doi: [10.1051/0004-6361/201628373](https://doi.org/10.1051/0004-6361/201628373)
- Rong, J., Qin, S.-L., Zapata, L. A., et al. 2016, *MNRAS*, 455, 1428, doi: [10.1093/mnras/stv2406](https://doi.org/10.1093/mnras/stv2406)
- Sakai, T., Sakai, N., Foster, J. B., et al. 2013, *ApJL*, 775, L31, doi: [10.1088/2041-8205/775/1/L31](https://doi.org/10.1088/2041-8205/775/1/L31)
- Sakai, T., Yanagida, T., Furuya, K., et al. 2018, *ApJ*, 857, 35, doi: [10.3847/1538-4357/aaadfd](https://doi.org/10.3847/1538-4357/aaadfd)
- Sánchez-Monge, Á., Beltrán, M. T., Cesaroni, R., et al. 2014, *A&A*, 569, A11, doi: [10.1051/0004-6361/201424032](https://doi.org/10.1051/0004-6361/201424032)
- Schuller, F., Menten, K. M., Contreras, Y., et al. 2009, *A&A*, 504, doi: [arXiv:0903.1369](https://arxiv.org/abs/0903.1369)
- Spezzano, S., Sipilä, O., Caselli, P., et al. 2022, *A&A*, 661, doi: [10.1051/0004-6361/202243073](https://doi.org/10.1051/0004-6361/202243073)
- Taniguchi, K., Guzmán, A. E., Majumdar, L., Saito, M., & Tokuda, K. 2020, *ApJ*, 898, 54, doi: [10.3847/1538-4357/ab994d](https://doi.org/10.3847/1538-4357/ab994d)
- Taniguchi, K., Herbst, E., Caselli, P., et al. 2019, *ApJ*, 881, doi: [10.3847/1538-4357/ab2d9e](https://doi.org/10.3847/1538-4357/ab2d9e)
- Taquet, V., López-Sepulcre, A., Ceccarelli, C., et al. 2015, *ApJ*, 804, 81, doi: [10.1088/0004-637X/804/2/81](https://doi.org/10.1088/0004-637X/804/2/81)
- Tercero, B., Cuadrado, S., López, A., et al. 2018, *A&A*, 620, L6, doi: [10.1051/0004-6361/201834417](https://doi.org/10.1051/0004-6361/201834417)
- van der Walt, S. J., Kristensen, L. E., Jørgensen, J. K., et al. 2021, *A&A*, 655, A86, doi: [10.1051/0004-6361/202039950](https://doi.org/10.1051/0004-6361/202039950)
- Xue, C., Remijan, A. J., Burkhardt, A. M., & Herbst, E. 2019, *ApJ*, 871, 112, doi: [10.3847/1538-4357/aaf738](https://doi.org/10.3847/1538-4357/aaf738)
- Yue, Y.-H., Qin, S.-L., Liu, T., et al. 2021, *ARA&A*, 21, doi: [arXiv:2010.10731](https://arxiv.org/abs/2010.10731)
- Zernickel, A., Schilke, P., Schmiedeke, A., et al. 2012, *A&A*, 546, A89, doi: [10.1051/0004-6361/201219803](https://doi.org/10.1051/0004-6361/201219803)